TubULAR: Tracking deformations of dynamic tissues and interfaces in 3D

Noah P. Mitchell[1,2,*] and Dillon J. Cislo[2,†]

[1]*Kavli Institute for Theoretical Physics, University of California Santa Barbara*
[2]*Department of Physics, University of California Santa Barbara*

A common motif in biology is the arrangement of cells into tube-like sheets, which further transform into more complex forms. Traditionally, analysis of tissues' dynamic surfaces has relied on inspecting static snapshots, live imaging of cross-sections, or tracking isolated cells in 3D. However, capturing the interplay between in-plane and out-of-plane behaviors requires following the full surface as it deforms and integrating cell-scale motions into collective, tissue-scale deformations. Here, we introduce an approach to build *in toto* maps of surface deformation, following tissue parcels in the material frame of reference. The Tube-like sUrface Lagrangian Analysis Resource ('TubULAR') provides an open-source MATLAB implementation whose functionality is accessible either as a standalone toolkit or as an extension of the ImSAnE package used in the developmental biology community. TubULAR provides a framework for linking in-plane and out-of-plane behaviors and decomposing complex deformation maps into elementary contributions defining physically meaningful signatures of motion. We underscore the power of our approach by analyzing shape change in the embryonic Drosophila midgut and beating zebrafish heart. In the midgut, our results link asymmetric constrictions to the increasing organ length and to patterned vorticity in the organ chambers. We then extract the dynamics of the beating zebrafish heart, constructing a mode-based description for the organ's beat cycle. The method naturally generalizes to *in vitro* and synthetic systems, such as stem cell models of tube development and deforming phase-separated interfaces.

INTRODUCTION

In biological and synthetic settings alike, the morphogenesis of tube-like sheets and films is driven by a dynamic interplay between in-plane and out-of-plane behaviors [1–8]. Tissue development is a particularly rich example of this interaction, in which the dynamics of shape generation are intertwined with mechanical forces, cellular fate, and organ function. In epithelia [9, 10], visceral organs [11, 12], vasculature [13], elastic shells [14], and whole organisms [15], quasi-2D surfaces deform in 3D space, contracting and dilating in-plane and bending out-of-plane in a coupled fashion. Understanding the dynamic mechanisms by which the systems change shape requires not only capturing instantaneous motion in 3D, but following the material as it deforms to build so-called 'Lagrangian' measures of deformation [16–18]. Furthermore, decomposing that motion into in-plane and out-of-plane components enables insights into the (bio)material's constitutive behavior, the processes generating its shape, and its physiological function [12, 19–21].

Much of of our understanding of morphogenesis built during the last century has relied on qualitative analysis of 2D live imaging and static snapshots of dynamic growth processes in 3D [22–24]. Emerging computational approaches in the life sciences have enabled quantitative characterizations that often challenge traditional assumptions and clarify the complex relationship between gene expression patterns, physical forces, and tissue geometry [4, 18, 25–28]. In a particularly fruitful methodological advance, the community has applied differential geometry techniques to establish 'tissue cartography' methods for mapping curved tissues to a planar representation, dramatically reducing the computational power required to track and store 3D data [29–31]. This framework has facilitated insights in a wide variety of systems including fly wings [32], eyes [33], and egg chambers [34], ascidian vasculature [35], zebrafish hearts [30] and endoderm [29], and mouse intestines [36]. By building on this theme, we implement automated methods for registering dynamic surfaces across time and classifying the signatures of tissue deformation. As shown in Fig. 1, this provides a framework for tracing the dynamics of complex shapes, leveraging the geometric constraints of tube-like topologies. Our toolkit provides a method to both construct and interpret Lagrangian measurements on dynamic surfaces.

By applying this approach to the developing embryonic digestive tract in the fly *Drosophila melanogaster* [12, 37–39] and the beating heart of the embryonic zebrafish *Danio rerio* [11, 21, 40–42], we extract the signatures of in-plane and out-of-plane tissue deformation. Focusing on the asymmetries in each system's dynamics, we obtain simple geometric principles underlying their shape change.

IMPLEMENTATION

TubULAR is publically available on GitHub, with documentation and example scripts at `https://npmitchell.github.io/tubular/`. A typical workflow passes through (1) level sets segmentation for surface detection, (2) generation of a pullback representation for surface parameterization and visualization, (3) flow analysis using TubULAR's discrete exterior

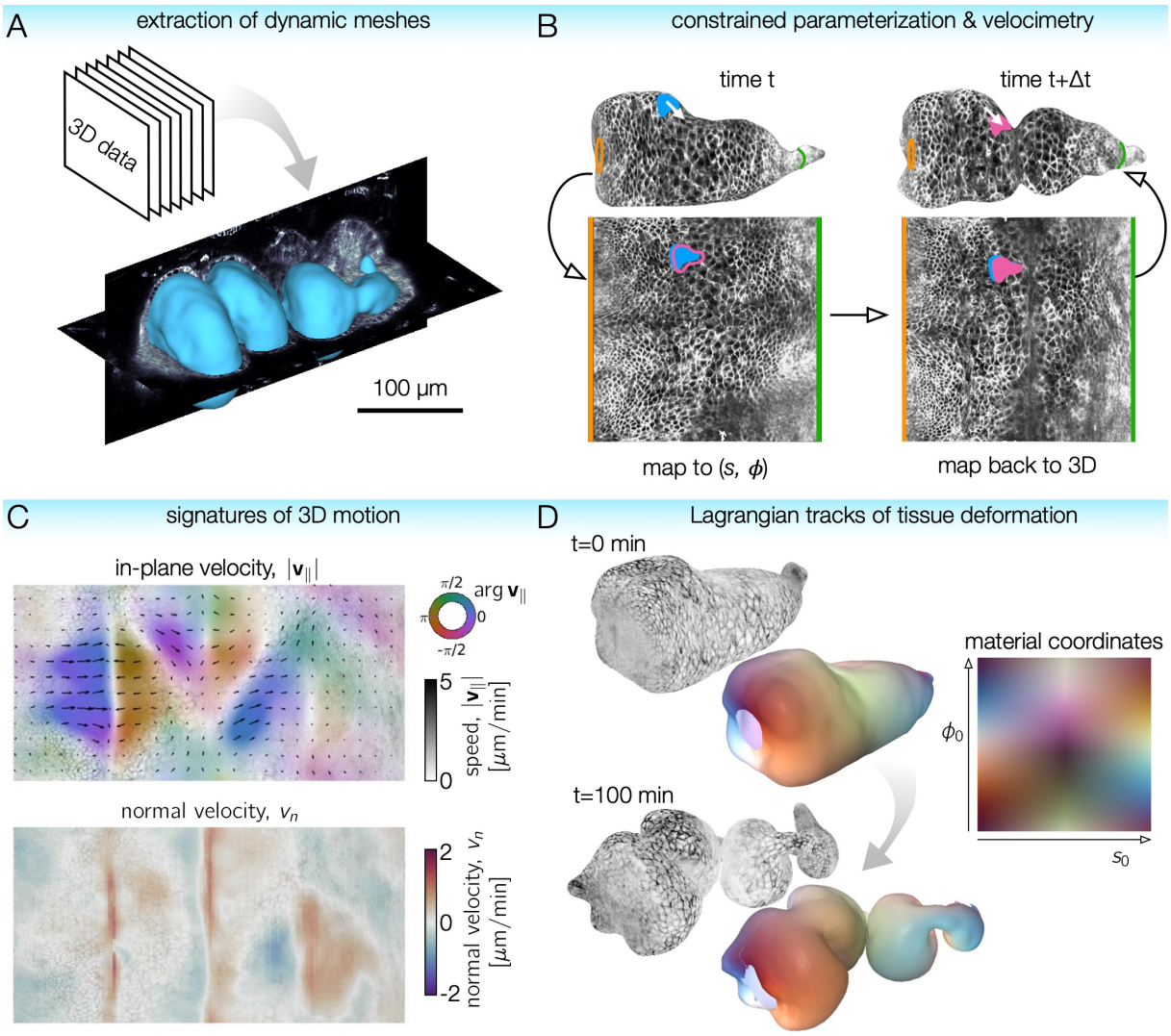

FIG. 1. **TubULAR is a toolkit for understanding the dynamics of evolving tube-like surfaces, such as visceral organs.** *(A)* TubULAR first extracts dynamic surfaces of interest from volumetric datasets. *(B)* Whole-surface parameterization using a generalized cylinderical coordinate system facilatates tracking tissue deformations. Since pullback images of adjacent timepoints are optimized to be nearly stationary in the parameterization space, 3D tissue velocities are obtained by linking the pre-image of the pullback coordinates across timepoints. *(C)* By extracting in-plane and out-of-plane tissue motion, TubULAR generates decomposition of the underlying motion, here shown by a 2D pullback representation of the in-plane tissue velocity $\mathbf{v}_{\parallel}$ (colored quiverplot) and the normal motion, v_n (red for inward velocity, blue for outward). *(D)* Finally, the toolkit tracks tissue deformations over time in the tissue's frame of reference (the Lagrangian frame). Here, a whole organ is colored by the location of each tissue parcel in its intrinsic material coordinate system (s_0, ϕ_0). As the tissue deforms during morphogenesis, patches retain their original color as they move, stretch, and bend.

calculus implementation, and (4) mode decomposition of the dynamics. In addition to the standalone toolkit, we are working to add the core functionality of TubULAR within the ImSAnE environment [30] for those in the community who are already comfortable with ImSAnE's workflow, to be available at `https://github.com/npmitchell/imsane`.

Contemporary microscopy methods used to probe living systems generate 3D volumetric data, wherein each voxel of the 3D data set corresponds to a (multi-channel) intensity measured at a specific location in the sample [43]. At the same time, many biological processes harness quasi-2D, thin tissues to sculpt complex 3D forms. To access the interplay between in-plane and out-of-plane dynamics in such systems, we must extract the tissue surface, track motion within the surface as it deforms, and decompose the resulting motion into signatures of deformation.

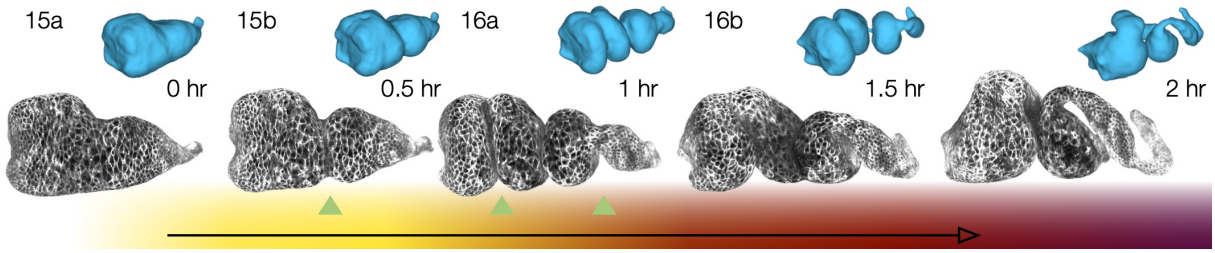

FIG. 2. **Computational microscopy enables dynamic tissue surface extraction.** Here, the endoderm tissue layer is selectively imaged for a *w;48Y GAL4 / UAS-CAAX::mCh* embryo. Morphogenesis proceeds first with a constriction partitioning the gut into two chambers (stage 15b, green arrow). Two more constrictions form a total of four chambers (16a, green arrows) before the gut begins to coil (16b) [12].

From volumetric data to dynamic textured surfaces

We first set out to identify and extract 2D surfaces of interest from 3D data. Surface detection and surface reconstruction are longstanding problems in the computer vision community and numerous methods have been built to address them in a variety of contexts [44, 45] . For the tube-like shape of the systems we address here, TubULAR effectively segments the data space into an 'inside' (i.e. everything within the tube) and an 'outside' (i.e. everything outside the tube), modulo the potentially necessary inclusion of virtual 'end caps' to close off the interior of an open tube. Exploiting this structural simplification, TubULAR employs a suite of level set segmentation methods designed to detect evolving tube-like surfaces. As illustrated in Fig. 1A, level set methods are a robust and powerful tool used to dynamically segment data volumes into complex watertight geometries whose boundaries are defined as the null contours of a signed distance function $u(\mathbf{x})$. The problem of surface detection is thereby reduced to optimizing the signed distance function so that $u(\mathbf{x}) = 0$ matches the tissue surface.

For clarity, we briefly summarize the morphological snakes level set method [46], one of the algorithms we have included with TubULAR. Here, the process of surface detection is mapped onto an optimization problem by defining a physics-inspired cost functional [46, 47]:

$$F[c_1, c_2, \mathcal{S}] = \mu \int_{\mathcal{S}} \mathrm{d}s + \nu \int_{\Omega} \mathrm{d}^3\mathbf{x} \tag{1}$$

$$+ \lambda_1 \int_{u>0} |I(\mathbf{x}) - c_1| \mathrm{d}\mathbf{x} + \lambda_2 \int_{u<0} |I(\mathbf{x}) - c_2| \mathrm{d}\mathbf{x}, \tag{2}$$

where c_1 and c_2 are the average values of the data inside and outside, respectively:

$$c_1(\mathcal{S}) = \langle I(\mathbf{x}) \rangle_{\text{inside}} \tag{3}$$

$$c_2(\mathcal{S}) = \langle I(\mathbf{x}) \rangle_{\text{outside}}. \tag{4}$$

The first term is a surface tension that tries to smooth out ruggedness in the surface. The second term is an effective pressure that penalizes blow up in the enclosed volume of the segmented regions. The final two attachment terms incorporate the actual measured data into the optimization procedure. The third term attempts to homogenize the intensities of voxels included in the interior of the segmented volume and the fourth term attempts to homogenize the intensities of the excluded voxels. Variation of this function with respect to the signed distance function yields the Euler-Lagrange equation [46]:

$$\partial_t u = |\nabla u| \left(\mu \nabla \cdot \left(\frac{\nabla u}{|\nabla u|} \right) - \nu \right.$$
$$\left. - \lambda_1 (I - c_1)^2 + \lambda_2 (I - c_2)^2 \right). \tag{5}$$

The solution of the optimization problem proceeds as follows. For the first time point, an initial guess is supplied for the signed distance function (e.g. a small sphere of $u = 1$ anywhere inside the tube). This field u evolves iteratively according to Eq. (5) until it fills the organ and further evolution no longer decreases the cost functional of Eq. (1). For subsequent time points, the previous solution is used as an initial guess, with appropriate erosion and smoothing steps to ensure stability of the scheme over time. The level set surface detection procedure can be performed directly on raw data or, alternatively, on the output of a pixel classifier [48]. This pre-processing can greatly reduce noise in the data and facilitate high quality surface extraction. TubULAR includes scripts designed to interface with the machine learning classification software iLastik for this pre-processing step [48].

Once a data volume corresponding to a particular time point has been segmented, the discrete surface is used to generate a mesh triangulation suitable for the subsequent discrete differential geometry calculations integral to the TubULAR workflow. The surface meshes can be generated by any of the surface reconstruction algorithms implemented in TubULAR, including marching cubes [49], advancing front [50], and Poisson surface reconstruction [51].

The final result is a dynamic set of surfaces tracing the tube-like surface over time, as illustrated in Fig. 2.

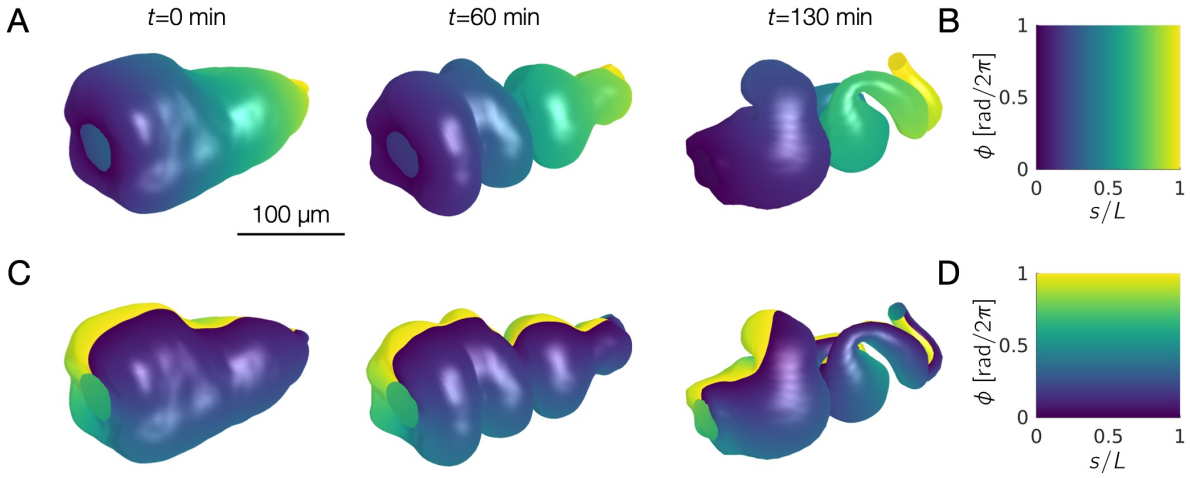

FIG. 3. **Coordinate parameterization follows 3D deformations of the evolving surface, shown here for the fly midgut as it folds into a coil of compartments.** *(A)* Rather than simply parameterizing the surface by coordinates in the Eulerian frame, here curves of constant s parameterize position along the organ's intrinsic longitudinal/AP axis, as computed via proper length along the surface. *(B)* A 2D pullback representation of the material frame reflects the longitudinal coordinates colored in (A). *(C)* Curves of constant ϕ denote position along the organ's circumferential/DV axis. *(D)* The longitudinal coordinate s measures the geodesic distance along the longitude of the tube-like surface. Colors correspond to the surfaces shown in (C).

A standalone toolkit for rendering the data onto the surface (as a 'texture') is included and implemented within TubULAR. Fig. 2 highlights the projection of volumetric data onto the surface for the case of a plasma membrane marker driven in the shape-changing, embryonic Drosophila midgut.

Constrained surface parameterization enables tracking deformation

Understanding the ways in which shape dynamics couple to biological processes such as cell shape change, intercalation, intracellular patterning, and gene expression requires the ability to identify and follow patches of tissue as they move and deform. On its own, the surface extraction procedure described in the previous section provides an instantaneous description of the surface geometry at each time point, but offers no way to consistently identify how particular patches of cells move and deform from time point to time point. The first major contribution of the TubULAR package is the ability to generate a set of time-dependent coordinate systems allowing for the calculation and analysis of physical observables taking into account tissue flow and deformation. In the language of continuum mechanics, we now seek to advance from an *Eulerian* description, wherein dynamical observables are measured at particular locations in space, to a *Lagrangian* description, wherein dynamical observables are queried by following material parcels along the surface as morphogenesis proceeds [52].

As shown in Fig. 3, we build a parameterization scheme such that the motion of the cells (or other objects) in the pullback representation move as little as possible. This enables us to easily follow a virtual representation of in-plane deformations in pullback space, which we can then project into 3D to follow the true motion. To this end, TubULAR's cartographic mapping functions first map the surface to the plane, then stabilize noise in the mappings' dynamics.

The parameterization process begins with the removal of a pair of 'end cap' regions at the poles of the extended, watertight meshes produced during surface extraction. For typical use cases, this converts a closed mesh with spherical topology to an open surface with cylindrical topology.

We then map the mesh into the plane for parameterization, cutting a virtual seam into the mesh so that the cylindrical mesh topology is can be 'unrolled' into the plane. To facilitate the analysis of anisotropic tissue deformations later in the pipeline, this mapping into the plane is always a *conformal* mapping, i.e. a totally isotropic, angle-preserving map. This conformal map is constructed either by discrete Ricci flow [53] (included as a custom package within TubULAR) or via minimizing the Dirichlet 'energy' of the mapping [54]. Inspired by the topology-preserving orbifold mappings of spherical surfaces [55], we also enforce a set of boundary conditions to ensure that the parameterization in the plane respects the cylindrical topology of the 3D surface. Namely, we demand continuity in the boundary components of the 2D meshes associated with the virtual seam, such that, if one were to tile these meshes in the plane, moving across this boundary from one tile into another would be

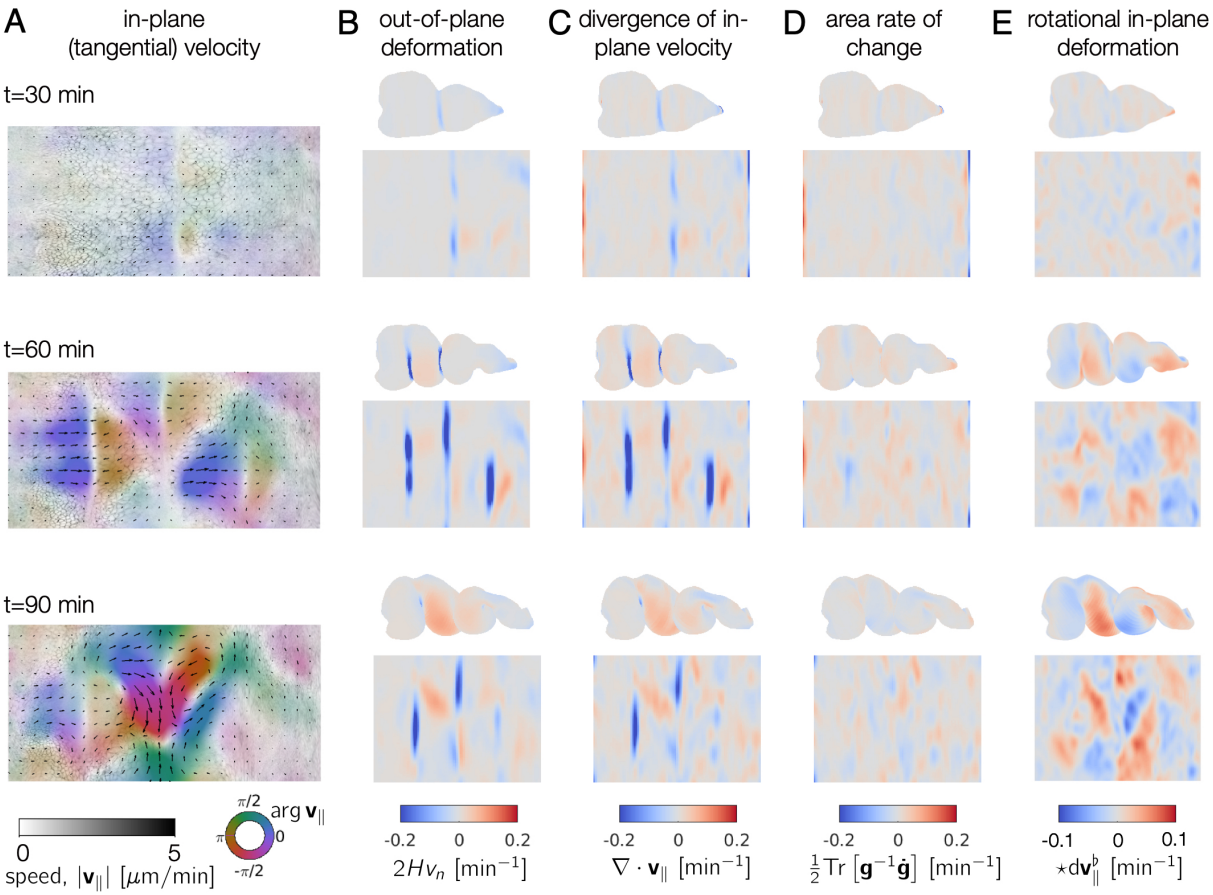

FIG. 4. **Discrete exterior calculus measurements of tissue velocity return signatures of motion.** *(A)* 2D pullback representation of in-plane (tangential) tissue motion shows a line defect near the middle constriction, then defects at the anterior and posterior constrictions, followed by increasingly complex in-plane flows. *(B)* The underlying out-of-plane deformation, defined as the normal motion v_n times twice the mean curvature $2H$, shows negative values at each constriction, where the mean curvature becomes negative. *(C)* DEC computation of the divergence of the in-plane velocity $\nabla \cdot \mathbf{v}_{\parallel}$ shows patterns of sinks in the constrictions and sources in the chambers' lobes, in synchrony with the out-of-plane deformation. *(D)* As a result of the match between in-plane and out-of-plane, the areal growth rate – defined as $\mathrm{Tr}\left[\mathbf{g}^{-1}\dot{\mathbf{g}}\right]/2$ – remains relatively quiescent. Here $\mathbf{g}$ is the first fundamental form of the tissue surface. *(D)* DEC computation of the rotational component of motion reveals vorticies of alternating sign along each lateral side. When viewed from the left, the rotation is negative for chambers 1 and 3 and positive for chambers 2 and 4. For this sign convention, positive rotational flow corresponds to a curl aligned with the inward surface normal.

physically indistinguishable from crossing over the virtual seam on the 3D cylindrical surface.

Finally, we wish to advance from this initial, conformal mapping to follow the tissue motion, warping the tissue parameterization onto the surfaces extracted in adjacent timepoints. Before doing so, we introduce an additional coordinate transformation which we have empirically found to improve the stabilization procedure. In particular, for tubes with large variations in effective radius along the length of the tube (such that the tube bulges and necks along its length), an additional quasi-conformal transformation (i.e. a smooth transformation with finite anisotropic distortion [56]) of the initial coordinates aids in subsequent stabilization. We denote this second planar pullback parameterization (s, ϕ), shown in the leftmost panels of Fig. 3. For the reference timestep considered first, the coordinate directions $(\hat{s}, \hat{\phi})$ are the same as the conformal mapping to the plane at a reference time $t = 0$. Furthermore, at this initial timepoint, ϕ is identical to the intrinsic circumferential axis of the conformal map. The sole difference is that s parameterizes a longitudinal position along the long axis of the organ at $t = 0$. In particular, we compute s as the average geodesic length along the surface from the anterior endcap to a set of uniformly-sampled points with fixed horizontal coordinate in the conformal pullback space (Fig. 3A-B). Intuitively then, s this is the average path length required to travel on the surface from the anterior face to a given location along curves of constant ϕ.

In subsequent timepoints, the difference in param-

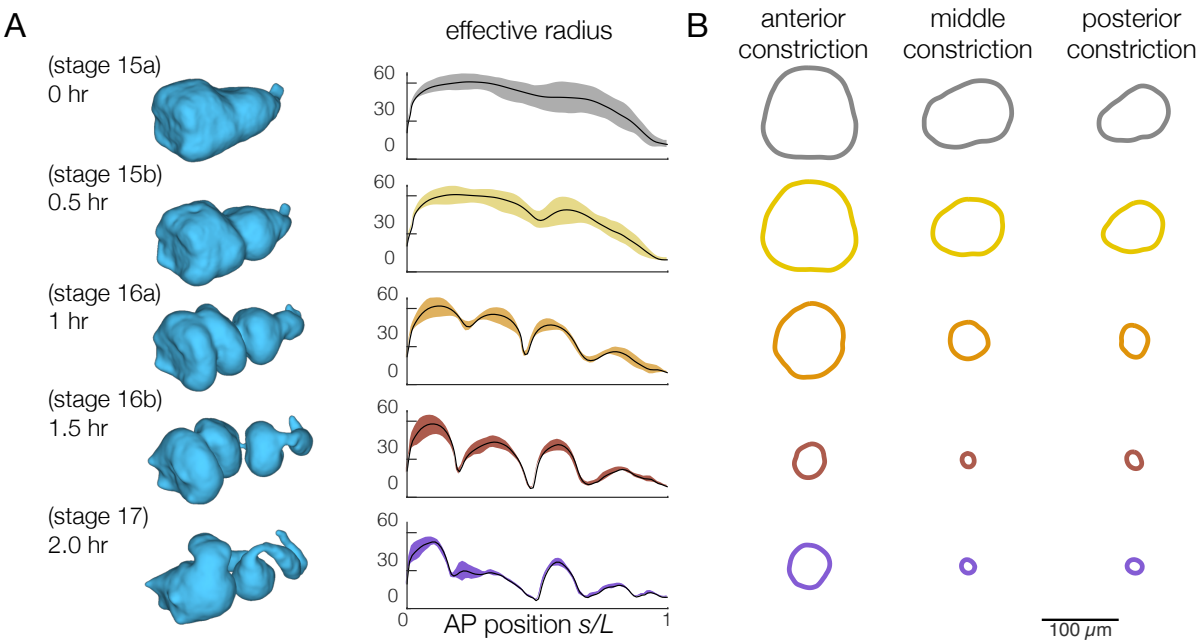

FIG. 5. **Computational sectioning of the midgut cross-sections shows that constrictions adopt circular shapes.** *(A)* Via whole-organ surface parameterization, we compute a cross-sectional width of the organ (effective radius) as a function of length, averaged over the circumference at each location along the intrinsic anterior-posterior axis of the organ surface (s, a measure of proper distance along the organ surface in the material frame). The shaded band represents the minimum and maximum effective radii along each circumferential hoop (s =constant). The narrow distribution in distances from the centerline to the constricting regions reflects the circular cross-sectional shape during constriction. *(B)* When viewed in their respective dynamic, tilting tangent planes, midgut constrictions are shown to adopt circular shapes as they tighten.

eterization coordinates in 3D space are minimized to match the previous timepoint, such that the coordinates follow the shape change of the organ. We find this (s, ϕ, t) parameterization aids in both visualization and enables more accurate velocimetry measurements than other choices we considered, particularly when large variations appear in the effective radius of the surface along its long axis. We are then able to follow extreme deformations of the tissue in 3D space simply by following gentle motions of the tissue in the pullback plane, as sketched in Fig. 1.

Centerline construction

Using the surface parameterization, TubULAR then computes an organ centerline by leveraging the surface parameterization in 3D space created from the previous step. Hoops for which s = constant define an effective circumference for increments along the length of the organ, and the average 3D position of each hoop defines its centerline point. Connecting mean points of adjacent hoops along the length of the organ defines the centerline of the object (brown curve in Fig. 6B).

Covariant measures of motion access signatures of deformation

In order to *interpret* the resulting tissue flows, we then decompose the velocity fields into their underlying components. A given parcel can move both along the surface and normal to the surface, and separating these motions is needed to parse whether tissue is rotating or shearing, contracting or dilating, and protruding or ingressing – and to find the spatiotemporal pattern in which these motifs occur. We therefore first project the velocities into normal (out-of-plane) and tangential (in-plane) components. Tangential velocities on a curved surface, however, are not as simple to understand as they are in flat space. In curved surfaces, parallel lines cross and diverge, and the orientation of a cell may change by simply travelling along 'straight' lines (geodesics). To deal with velocity fields on curved surfaces, then, requires certain computational tools, which we detail below. The default implementation in a TubULAR pipeline is to (1) extract the in-plane divergence, curl, and Laplacian of tissue velocity, and (2) relate the in-plane divergence to the out-of-plane motion v_n to determine the rate of areal growth across the surface (see Fig. 2 and [12]).

These calculations rest on an implementation of the discrete exterior calculus (DEC) formalism [57, 58], which we have included with TubULAR, and which func-

tions on its own as a standalone toolkit. The DEC is a simple and flexible framework offering a unified platform for discrete geometry processing (see documentation at `https://npmitchell.github.io/tubular/DEC.html`). Signals are represented as discrete differential forms on the simplicial structure of the triangulated mesh which yield natural definitions for linear differential operators. These basic operations can be combined together to form covariant representations of more complicated differential operators, including the divergence, curl, and Laplacian operators that are a part of TubULAR's default workflow. These operators can be directly applied to geometric data (e.g. surface curvature), kinematic data (e.g. surface velocities), and beyond (e.g. surface data intensity, surface data anisotropy fields etc.) to understand the ways in which spatiotemporal variation in observable fields generate 3D shape change. Advanced users of the TubULAR system can use them to construct soluble discrete representations of physical models (e.g. the Navier-Stokes equations on a surface [59, 60]) and directly test their predictions on evolving non-trivial geometries.

In order to make these methods accessible to the broadest possible audience, we have packaged all of this functionality within an easy to operate functional user interface. No deep knowledge of differential geometry or exterior calculus is necessary to use our implementation of the DEC. For those who are interested, a brief, but more comprehensive, description of the methods is contained within the SI and the online documentation.

Fig. 4 displays examples of these calculations applied to the developing fly midgut. Whole-organ measurements of the tangential velocity are represented in the 2D pullback coordinates for snapshots of a representative embryo in Fig. 4A. The orientation of flow relative to the longitudinal axis $\hat{s}$ is denoted by color and the magnitude of the motion reflected by opacity and arrow length. Further processing via DEC of the in-plane velocity fields show that out-of-plane deformation ($2Hv_n$) is tightly linked to localized sinks in the flow ($\nabla \cdot \mathbf{v}_{\parallel} < 0$) near constrictions, and positive out-of-plane deformation is likewise linked to sources in the in-plane flow ($\nabla \cdot \mathbf{v}_{\parallel} > 0$), as shown in Fig. 4B-C. Here, v_n is the normal velocity and H is the mean curvature of the surface. The kinematic consequence of the close match between these two fields is a quiescent rate of areal change of the tissue. In other words, despite the fact that in-plane tissue flow and out-of-plane motion are large, their signatures match so as to nearly preserve tissue area during deformation (Fig. 4D, see also [12]). The rotational component of the flow, meanwhile, adopts a pattern of vorticity in the lateral faces of each lobe, with alternating sign (Fig. 4E), a feature we will discuss in a later section.

Lagrangian measures of time-integrated tissue strain

Endowing the evolving surface with a set of Lagrangian coordinates enables the construction of a *material metric*. The metric tensor, $\mathbf{g}(t)$, is a geometric object enabling the measurement of distances and angles between nearby points on the surface. The rate-of-deformation tensor describes how lengths and angles change locally as the surface deforms in time:

$$\frac{dg_{ij}(t)}{dt} = \nabla_i v_j + \nabla_j v_i - 2\, v_n\, b_{ij}, \tag{6}$$

where v_i, $i \in \{1, 2\}$, and v_n denote the tangential and normal components, respectively, of the Lagrangian surface velocity, ∇_i denotes the covariant derivative with respect to the ith tangential coordinate, and b_{ij} denote the components of the second fundamental form – another geometric tensor object that measures surface curvature. Essentially, Eq. (6) tells us that lengths and angles deform under the surface motion when there are gradients in the tangential velocity *and/or* when there is normal motion in curved regions of the tissue. We can then integrate the rate-of-deformation tensor along pathlines to construct a Lagrangian measurement of cumulative tissue strain, i.e.

$$\varepsilon(t) = \frac{1}{2} \int_{\tau=0}^{\tau=t} d\tau\, \frac{d\mathbf{g}(\tau)}{d\tau} = \frac{1}{2}\left(\mathbf{g}(t) - \mathbf{g}(0)\right). \tag{7}$$

In the language of geometric elasticity, this is equivalent to the Green-St. Venant strain tensor [61], defined relative to the 'undeformed' reference configuration at time $t = 0$.

Tensor field decomposition simplifies complicated deformations

Frequently, seemingly complicated patterns of motion can be decomposed into a sum of contributions from simpler components. This strategy has been successfully adopted in various contexts within morphogenesis, including analysis of the complicated tissue motions observed in zebrafish gastrulation [62] and in reconstructing the 4D growth patterns generating vertebrate limbs [63]. The TubULAR package includes a variety of methods for deconstructing complex observable fields into elementary components.

We include the capability to decompose surface vector fields (e.g. material tissue velocities) into their geometric components. First, surface vector fields are separated into their normal and tangential components. Next, our implementation of the DEC includes a simple interface to generate a Helmholtz-Hodge decomposition of tangential vector fields [58], i.e. a decomposition into dilatational, rotational, and harmonic parts. This procedure explicitly determines the relative contribution of the geometric

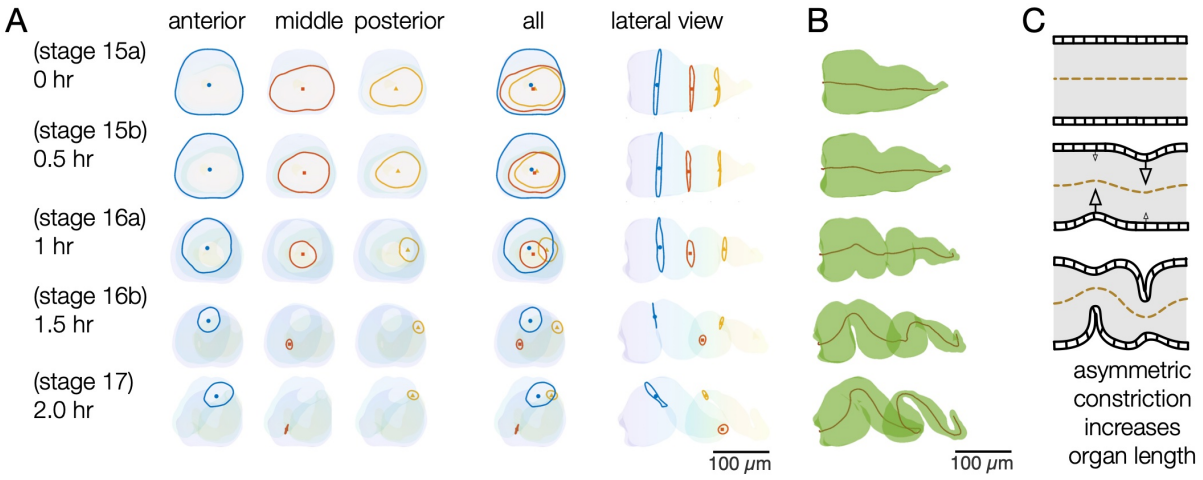

FIG. 6. **Midgut constrictions are not co-axial, with the anterior constriction pulled dorsally and the posterior constriction pulled toward the left dorsolateral direction.** *(A)* Constriction asymmetries are highlighted when viewing the organ along the anterior-posterior axis of the embryo (in the Eulerian frame). Note that unlike in Fig. 5, here we do not rotate into the local transverse plane of each constriction. Positions of each constriction are marked in blue (anterior constriction), red (middle constriction), and yellow (posterior constriction). *(B)* Constriction asymmetries in the transverse plane of the organ generate effective length increase of the organ, as measured by the centerline (brown curve). *(C)* Purely geometrically, an asymmetric constriction lengthens an organ centerline as an asymmetric fold deepens.

signatures of the in-plane flow to the out-of-plane deformation.

TubULAR also includes functionality to construct simple mode decompositions of arbitrary tensor fields on the surface. This functionality comes in two forms. First, our DEC implementation decomposes signals onto a basis of the eigenfunctions of the discrete Laplace-Beltrami operator [64]. More simply, this compares the relative importance of long-wavelength modes (with smooth spatial variation) and short-wavelength modes (with rapid spatial variation) in generating the observed signals. Second, we include functions to decompose signals using principal component analysis (PCA) [65]. This type of analysis lets users extract more general patterns of motion that contribute most strongly to the variance observed across time or across datasets.

APPLICATION TO THE DROSOPHILA MIDGUT

We now leverage the TubULAR toolkit to investigate the role of dorso-ventral asymmetries in early Drosophila midgut morphogenesis. We find that midgut constrictions are highly circular, but that the position of these circular constrictions are not co-axial (c.f. [66, 67]). Together, these observations provide a geometric basis not only for the elongation of the organ, but also for rotational flows in the chambers between constrictions. They additionally raise questions about the mechanical underpinnings of uniform cross-sectional shape in the midst of anisotropic displacement.

Gut constrictions are circular despite initially anisotropic shape

During embryonic development in Drosophila, heterologous tissue layers come together to form the digestive tract. The middle portion of this digestive system is known as the midgut, which connects to the foregut and the hindgut [68]. The tissues that form the gut first straddle the yolk near the center of the embryo before migrating dorsally and ventrally, closing into a tube-like shape, with a layer of muscle cells ensheathing an endodermal monolayer [39, 66, 68–70].

After the midgut first closes into a tube, the organ takes on a rectangular shape in its anterior and tapers to an asymmetric elliptical shape towards the posterior. Subsequently, the midgut forms a constriction midway along its length, then two more constrictions subdividing the organ into four chambers [12, 37]. Using the computational sectioning offered by TubULAR's surface parameterization, we find that though the gut tube initially has rectangular and irregular cross sections at constriction precursors, the constrictions rapidly adopt circular cross sections to within 10% of the radius, as shown in Fig. 5. This tightening of the cross-sectional geometry suggests that the tension is uniform throughout the DV direction, consistent with a model in which the highly elongated circular visceral muscles driving force generation during this process (c.f. [12, 66]).

To perform these measurements, we define an effective radius as the average distance from each point in a uniform sampling of a ring of constant s (computed via the mapping to the pullback plane) to the centerline, which

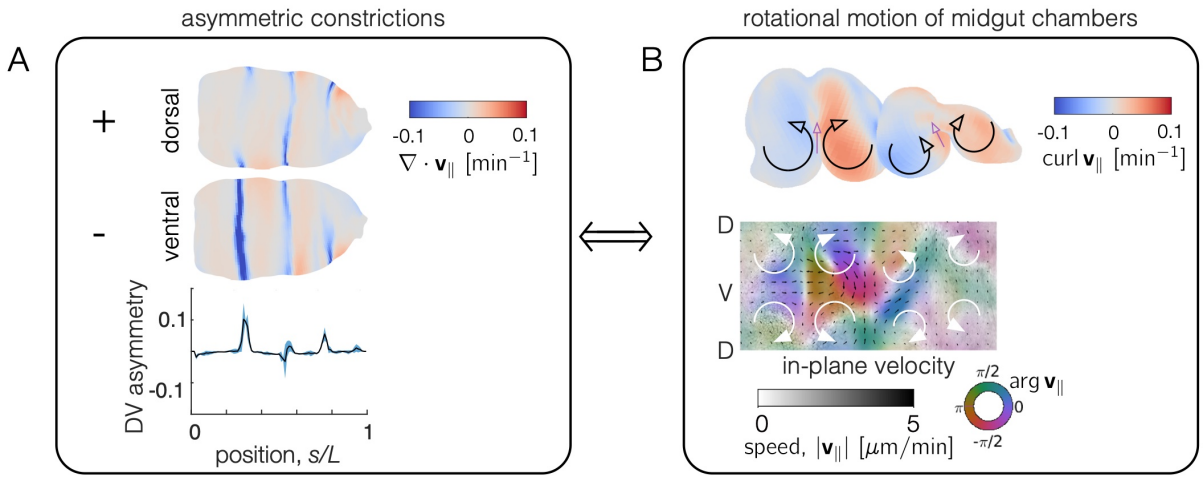

FIG. 7. **Dorsal-ventral asymmetry in midgut constrictions is linked to rotational motion of gut chambers in 3D.** *(A)* The dilatational component of the in-plane motion – that is, the in-plane divergence – shows localized sinks at each constriction, but these sinks are preferentially strong on the ventral side of the organ for the anterior and posterior constrictions. Here, we map the average divergence measured during the first 90 minutes after the onset of the middle constriction in the Lagrangian frame, visualized in 3D. The divergence is averaged over the dorsal and ventral halves of each circumferential ring, and the ventral mean is subtracted from the dorsal. We plot the difference against the anterior-posterior position, s, which parameterizes the geodesic distance (pathlength) from the anterior face averaged over the circumferential coordinate, ϕ. *(B)* The rotational component of in-plane velocity, computed via DEC, registers counter-rotating vortices in the lateral faces of the gut chambers. In the 2D pullback projection, this motion forms hyperbolic swirls, reminiscent of the polonaise motions seen in vertebrate gastrulation and Drosophila germ band extension.

is composed of the mean positions of all circumferential rings. We then identified constriction locations as rings of constant s whose effective radii $r(s)$ are local minima (so that $\partial_s r(s) = 0$). Local minima in effective radius are tracked starting at the onset of folding forward in time to define constriction locations. Before the onset of folding, presumptive constriction locations are inferred by back-tracing the onset location to earlier timepoints.

Midgut constrictions are not co-axial, thereby elongating the organ

Though the constrictions are circular, the radial tissue displacement during folding is azimuthally symmetric only for the middle fold during the first hour. As shown in frontal views in Fig. 6A, the anterior constriction marches dorsally, while the posterior constriction pulls to the left. Thereafter, the anterior and posterior constrictions continue to move distally and the middle constriction loses its initial axial symmetry. In summary, these constrictions are not co-axial along the AP axis of the organ (or of the embryo as a whole).

We find that this asymmetry in the distal positioning of the constrictions during morphogenesis generates elongation of the organ. Using TubULAR to compute the midgut centerline throughout morphogenesis, we see that the initially straight centerline elongates when viewed from the lateral side as a consequence of the dorso-ventral asymmetry of the anterior and posterior constrictions (Fig. 6B), To understand the geometric principle behind this statement in its simplest form, consider a straight tube sketched in Fig. 6C. As constrictions form preferentially on the ventral and dorsal sides, the centerline of the organ must extend if the endpoints are fixed. This highlights a simple geometric mechanism in which developing organs can increase their effective length via asymmetric morphogenesis, which may be useful for physiological purposes like efficient digestion. As described in [12], a similar geometric principle extends also to the length along the surface of the organ if the surface area of the organ is locally preserved.

Midgut constriction asymmetry is linked to polonaise motions in the tissue deformation

Fig. 7A displays the dorsal-ventral asymmetry in the in-plane instantaneous contractile flows in the Lagrangian frame, averaged over the first 90 minutes of morphogenesis for a representative embryo. The DV asymmetry is then computed from such velocity-fate maps as the difference between the dorsal and ventral signatures of $\nabla \cdot \mathbf{v}_{\parallel}$ for three embryos aligned in space and time. Both the anterior and posterior constrictions register a positive-valued peak in the asymmetry, implying that the sinking divergence is weaker on the dorsal side. Due to the tissue's kinematic coupling between in-plane and out-of-plane motion [12], this asymmetric motion is linked to asymmetric out-of-plane deformation with high fidelity.

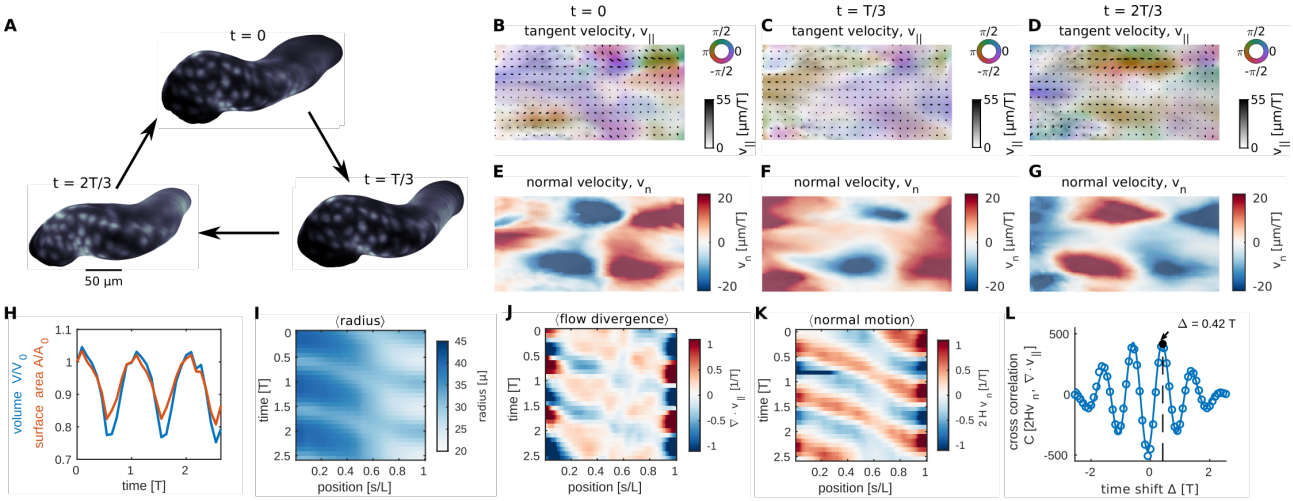

FIG. 8. **Tracing the in-plane and out-of-plane dynamics of a beating reveals the phased coupling between dilatational and transverse deformations.** *(A)* Segmentation of a beating zebrafish heart shows cyclic deformations in 3D. *(B-G)* Decomposing tissue motion into in-plane and out-of-plane demonstrates how pulsed deformation travels along the long axis of the tube, from the atrium to ventricle. *(H)* Relative change in the total enclosed volume and surface area over time. *(I)* Kymograph of the distance from the surface to the centerline averaged along the circumferential axis. *(J-K)* Kymographs of in-plane and out-of-plane motion averaged along the circumferential axis of the tube highlights non-reciprocal dynamics. *(L)* Because of the phase difference between in-plane motion and out-of-plane deformation, cross correlation of the two motions indicates an offset phase relationship between the two. The curve shown is a fit to the data by an offset sinusoidal wave with a Gaussian amplitude envelope.

How does this asymmetry in in-plane divergence link, in turn, to the rotational motion?

We find that constrictions' asymmetry couples to rotational motion in the midgut chambers, as shown in Fig. 7B. Using TubULAR to identify the rotational component of deformation in the Lagrangian frame, we find that as constrictions deepen, the lateral sides of the chambers begin to show a pattern of vorticity with alternating signs along both axes of the organ (see also Fig. 4E). As highlighted in Fig. 7B, the dorso-ventral asymmetry of the anterior and posterior constrictions generate broadly distributed vorticity in the lateral sides of the chambers – akin to solid body rotation of the lateral faces – with alternating sign in adjacent chambers. In the 2D pullback representation, the resulting flows form counter-rotating swirls, reminiscent of the 'polonaise' motion of primitive streak formation and germ band extension during early embryogenesis [17, 26, 71].

DECOMPOSING DEFORMATIONS DURING HEART MORPHOGENESIS

To test the generality of the method and extend our analysis to shapes with cyclic deformations, we analyzed a beating zebrafish heart during during the second day of development post fertilization. *In toto* imaging of the heart relied on light-sheet illumination of a transgenic Tg(*cmlc2:eGFP*) embryo expressing GFP in cardiomyocytes [72]. These data were taken using a temporal supperresolution approach [42], in which acquisition was synchronized with the beating of the developing heart to build volumetric data at 11 equally-spaced phases of the heart beat cycle. The 3D shape of the beating heart is shown for a set of illustrative time points in Fig. 8A. Passing the volumetric data through TubULAR returns covariant measures of in-plane and out-of-plane deformation.

Beating heart exhibits a phase delay between in-plane motion and out-of-plane deformation

Cyclic deformations of the heart result in in-plane velocities $\mathbf{v}_{\parallel}$, colored by their orientation in Fig. 8B-D and out-of-plane motion v_n that constricts or dilates the tube Fig. 8E-G. The extracted heart shape changes both surface area and volume as it beats, shown in Fig. 8H. We highlight the waveform of the beat by plotting a kymograph of the radius as a function of time and position along the long axis of the tube in Fig. 8I. In this measurement, we average along the circumferential axis of the tube, given that the developing heart is reasonably symmetric along its circumference at this stage.

Unlinke in midgut morphogenesis, the beating heart's in-plane velocities are not directly correlated with the out-of-plane deformation so as to produce incompressible motion. While both the in-plane divergence and out-of-plane motion display directional waves in their kymographs, the two fields are out of phase. As shown

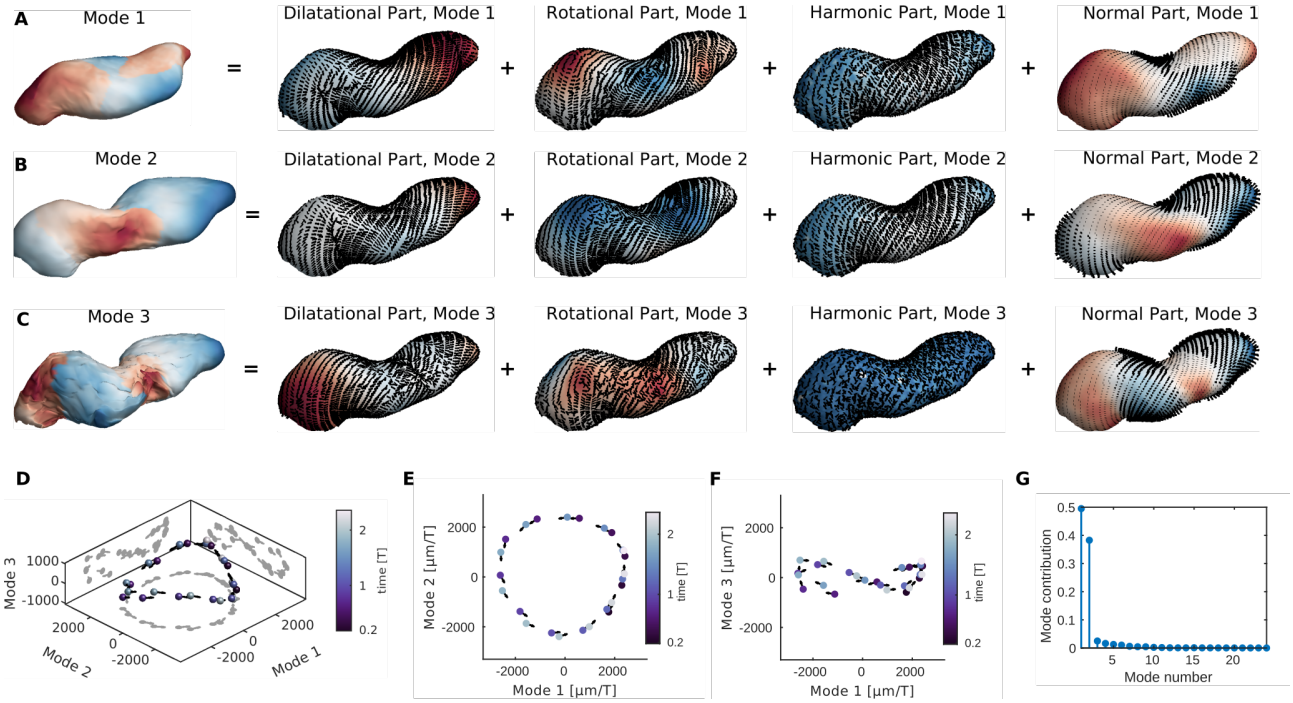

FIG. 9. **Decomposition of tissue motion in the beating heart reveals two principal components with non-reciprocal dynamics.** *(A-C)* Visualization of the principal components of Lagrangian tissue velocities. The first image in each panel shows the deformation induced by moving along the associated component axis, colored by the alignment of the component axis with the surface normal direction. Subsequent images illustrate the Helmholtz-Hodge decomposition of the tangent part of the mode and also the normal part of the mode. Color in the dilatational part, rotational par, and harmonic part are given by the scalar potential, vector potential, and norm of the harmonic mode respectively. Color in the normal part is given by the norm of the normal component of the mode. *(D-F)* Principal component analysis on the time course of deformations returns two dominant modes of deformation with a phase relationship of nearly $\pi/2$, such that the system winds in state space along a nearly planar, circular pattern. *(G)* A comparison of the relative contribution of the first 24 modes. Mode contribution is defined as the time averaged ratio of the squared length of the projection of the velocity along each mode normalized by the total squared length of each velocity vector in state space.

in Fig. 8L, we measure a phase offset between the two fields of $0.42\,T$, where T is the period of heart beating. In other words, when the in-plane divergence is compressive at a given position on the curved tube, the normal motion expands the tube rather than constricts. This feature contrasts sharply with the irreversible constrictions of the fly midgut during embryonic stages 15-16, in which nearly incompressible kinematics lead to a 97% correlation between the two fields [12].

Mode decomposition of the heart reveals two out-of-phase characteristic deformations.

We applied TubULAR's mode decomposition tools to extract the extent to which the complex cyclic beating of the embryonic zebrafish heart can be explained by simpler constituent motions. In order to do so, the 3D Lagrangian tissue velocities were first lifted to reside in a high-dimensional space where each point was defined by the set of all velocities on the surface at a given time point. We then performed principal component analysis (PCA) to determine the axes in this high-dimensional space that explained the majority of the variance in the data over time. The three most important modes are displayed in Fig. 9A-C. We performed a Helmholtz-Hodge decomposition of the mode velocities using the built-in functionality of the DEC package contained in TubULAR to probe the signatures of motion contributing to each mode. We note that the two most important modes are relatively smooth, while the third mode is rugged and exhibits rapid variation over the surface (a trend that is exacerbated in higher-order, less important modes).

We then investigated the dynamics of the system when projected onto the 2D subspaces spanned by pairs of the three principal components Fig. 9D-F. While all pairings of course exhibit the same periodic behavior as the full motion, the shape of the orbits traced out in these configuration subspaces are markedly different for the first and second mode than for other pairings, including higher-order modes not shown. In particular, as shown in Fig. 9E, the system oscillates between the first two modes, sweeping out a roughly circular trajectory sub-

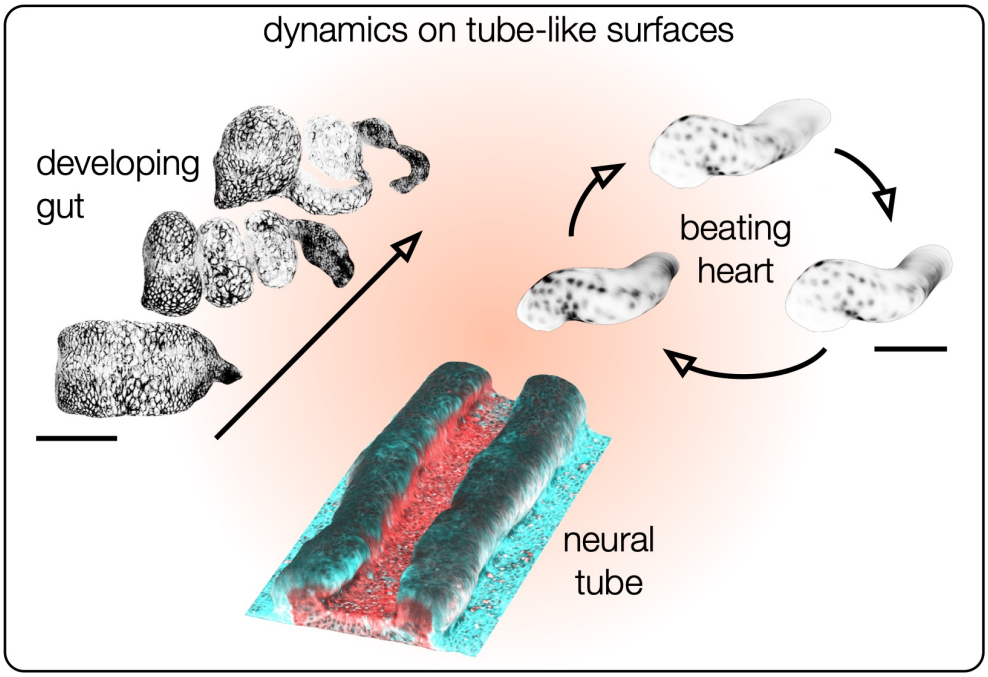

FIG. 10. **Dynamically deforming tubes is a common motif in biology.** Here, three developing organs are rendered on extracted surfaces: a Drosophila midgut [12], a beating zebrafish heart [42], and an *in vitro* neural tube growing in a dish from human stem cells [2].

tending a nonzero area. Other pairings, in contrast, generate trajectories that subtend balanced virtually zero area (Fig. 9D and F). This phased oscillation between the first two principal components highlight that unidirectional pumping of the heart is well-captured by a 2D state representation. This is also corroborated by the calculation of the contribution of each mode to the total motion shown in Fig. 9G, which shows that the first two modes capture nearly 90% of the deformation.

CONCLUSION

We have developed a computational framework for unravelling the complex, dynamic shapes of tube-like surfaces into their principal signatures of deformation, providing a documented, open-source MATLAB implementation to the community. Our implementation unifies the core elements of this toolkit with the existing ImSAnE package [30]. This framework computes Lagrangian measures of strain and strain rate, decomposing dilatational and rotational signatures and mapping them onto the a reference material configuration. Using this approach, we characterized the dorsal-ventral asymmetries during midgut constrictions, linking asymmetric out-of-plane motions to organ elongation and rotational tissue flows. We then characterized the cyclic deformations of the beating zebrafish heart, highlighting a phase difference between in-plane motion and out-of-plane deformation. We then captured the heart's directional pumping motion with a two-dimensional principal component analysis. As sketched in Fig. 10, an efficient method for tracing surface dynamics in the Lagrangian frame of reference offers new opportunities for understanding organoid systems as well, illustrated by the surface representation of a developing neural tube derived from human stem-cells [2].

ACKNOWLEDGEMENTS

We thank Sebastian Streichan and Boris Shraiman for insight, discussions, and mentorship. We thank Sebastian Streichan for supplying the light sheet dataset of the beating zebrafish heart and Eyal Karzbrun for supplying the confocal dataset of an *in vitro* neural tube. This research was supported in part by NSF Grant No. PHY-1748958 and the Gordon and Betty Moore Foundation Grant No. 2919.02. NPM acknowledges support from the Helen Hay Whitney Foundation.

* npmitchell@kitp.ucsb.edu; Corresponding author; Equal contribution
† djcislo@ucsb.edu; Corresponding author; Equal contribution

[1] B. Lubarsky and M. A. Krasnow, Cell **112**, 19 (2003).

[2] E. Karzbrun, A. H. Khankhel, H. C. Megale, S. M. K. Glasauer, Y. Wyle, G. Britton, A. Warmflash, K. S. Kosik, E. D. Siggia, B. I. Shraiman, and S. J. Streichan, Nature **599**, 268 (2021).

[3] K. Ivanovitch, S. Temiño, and M. Torres, eLife **6** (2017), 10.7554/elife.30668.

[4] J. F. Le Garrec, J. N. Domínguez, A. Desgrange, K. D. Ivanovitch, E. Raphaël, J. A. Bangham, M. Torres, E. Coen, T. J. Mohun, and S. M. Meilhac, Elife **6** (2017), 10.7554/eLife.28951.

[5] S. Brandstaeter, S. L. Fuchs, R. C. Aydin, and C. J. Cyron, GAMM-Mitteilungen **42**, e201900001 (2019).

[6] W. M. van Rees, E. Vouga, and L. Mahadevan, Proceedings of the National Academy of Sciences **114**, 11597 (2017).

[7] Y. Klein, E. Efrati, and E. Sharon, Science **315**, 1116 (2007).

[8] E. Sharon and E. Efrati, Soft Matter **6**, 5693 (2010).

[9] E. Hannezo, B. Dong, P. Recho, J.-F. Joanny, and S. Hayashi, Proceedings of the National Academy of Sciences **112**, 8620 (2015).

[10] E. Hannezo, J. Prost, and J.-F. Joanny, Proceedings of the National Academy of Sciences **111**, 27 (2014).

[11] J. Bakkers, Cardiovasc Res **91**, 279 (2011).

[12] N. P. Mitchell, D. Cislo, S. Shankar, Y. Lin, B. I. Shraiman, and S. J. Streichan, bioRxiv (2021), 10.1101/2021.11.07.467658.

[13] S. I. Rubinow and J. B. Keller, Journal of theoretical biology **35 2**, 299 (1972).

[14] E. Efrati, E. Sharon, and R. Kupferman, Soft Matter **9**, 8187 (2013).

[15] Y. Maroudas-Sacks, L. Garion, L. Shani-Zerbib, A. Livshits, E. Braun, and K. Keren, Nature Physics **17**, 251 (2021).

[16] M. Serra, S. Streichan, M. Chuai, C. J. Weijer, and L. Mahadevan, Proceedings of the National Academy of Sciences **117**, 11444 (2020).

[17] M. Saadaoui, D. Rocancourt, J. Roussel, F. Corson, and J. Gros, Science **367**, 453 (2020).

[18] M. Lefebvre, N. Claussen, N. Mitchell, H. Gustafson, and S. Streichan, bioRxiv , 10.1101/2022.01.12.476069 (2022).

[19] T. Lecuit and P.-F. Lenne, Nature Reviews Molecular Cell Biology **8**, 633–644 (2007).

[20] A. Mietke, F. Jülicher, and I. F. Sbalzarini, Proceedings of the National Academy of Sciences **116**, 29 (2019).

[21] A. S. Forouhar, M. Liebling, A. Hickerson, A. Nasiraei-Moghaddam, H.-J. Tsai, J. R. Hove, S. E. Fraser, M. E. Dickinson, and M. Gharib, Science **312**, 751 (2006).

[22] M. J. F. Barresi and S. F. Gilbert, *Developmental Biology* (Oxford University Press, 2020) p. 758.

[23] M. Levin, R. L. Johnson, C. D. Sterna, M. Kuehn, and C. Tabin, Cell **82**, 803–814 (1995).

[24] C. Nüsslein-Volhard and E. Wieschaus, Nature **287**, 795 (1980).

[25] T. Savin, N. A. Kurpios, A. E. Shyer, P. Florescu, H. Liang, L. Mahadevan, and C. J. Tabin, Nature **476**, 57 (2011).

[26] S. J. Streichan, M. F. Lefebvre, N. Noll, E. F. Wieschaus, and B. I. Shraiman, eLife **7** (2018), 10.7554/elife.27454.

[27] R. Etournay, M. Popović, M. Merkel, A. Nandi, C. Blasse, B. Aigouy, H. Brandl, G. Myers, G. Salbreux, F. Jülicher, and S. Eaton, eLife **4** (2015), 10.7554/elife.07090.

[28] C. Wolff, J.-Y. Tinevez, T. Pietzsch, E. Stamataki, B. Harich, L. Guignard, S. Preibisch, S. Shorte, P. J. Keller, P. Tomancak, and A. Pavlopoulos, eLife **7**, e34410 (2018).

[29] B. Schmid, G. Shah, N. Scherf, M. Weber, K. Thierbach, C. P. Campos, I. Roeder, P. Aanstad, and J. Huisken, Nature Communications **4**, 2207 (2013).

[30] I. Heemskerk and S. J. Streichan, Nature Methods **12**, 1139 (2015).

[31] S. Herbert, L. Valon, L. Mancini, N. Dray, P. Caldarelli, J. Gros, E. Esposito, S. L. Shorte, L. Bally-Cuif, N. Aulner, R. Levayer, and J.-Y. Tinevez, BMC Biology **19** (2021).

[32] Z. Zhou, H. Alégot, and K. D. Irvine, Current Biology **29**, 856 (2019).

[33] K. D. Gallagher, M. Mani, and R. W. Carthew, eLife **11** (2022), 10.7554/eLife.72806.

[34] W. Dai, X. Guo, Y. Cao, J. A. Mondo, J. P. Campanale, B. J. Montell, H. Burrous, S. Streichan, N. Gov, W.-J. Rappel, and D. J. Montell, Science **370**, 987 (2020).

[35] R. Madhu, D. Rodriguez, C. Guzik, S. Singh, A. W. De Tomaso, M. T. Valentine, and D. Loerke, Molecular Biology of the Cell **31**, 1714 (2020).

[36] A. Candeo, I. Sana, E. Ferrari, L. Maiuri, C. D'Andrea, G. Valentini, and A. Bassi, Journal of Biomedical Optics **21**, 1 (2016).

[37] K. Immerglück, P. A. Lawrence, and M. Bienz, Cell **62**, 261 (1990).

[38] M. Bienz and G. Tremml, Nature **333**, 576 (1988).

[39] M. Bienz, Seminars in Cell Developmental Biology **7**, 113 (1996).

[40] S. Bhat, J. Ohn, and M. Liebling, IEEE Transactions on Image Processing **21**, 3638 (2012).

[41] D. Stainier, R. Lee, and M. Fishman, Development **119**, 31 (1993), https://journals.biologists.com/dev/article-pdf/119/1/31/1124932/31.pdf.

[42] K. G. Chan, S. J. Streichan, L. A. Trinh, and M. Liebling, IEEE Transactions on Computational Imaging **2**, 348 (2016).

[43] U. Krzic, S. Gunther, T. E. Saunders, S. J. Streichan, and L. Hufnagel, Nature Methods **9**, 730 (2012).

[44] S. J. Osher and R. Fedkiw, *Level set methods and dynamic implicit surfaces.*, Applied mathematical sciences, Vol. 153 (Springer, 2003) pp. I–XIII, 1–273.

[45] A. Maiti and D. Chakravarty Background, SpringerPlus (2016), 10.1186/s40064-016-2425-9.

[46] P. Marquez-Neila, L. Baumela, and L. Alvarez, IEEE Transactions on Pattern Analysis and Machine Intelligence **36**, 2 (2014).

[47] T. F. Chan and L. A. Vese, IEEE Transactions on Image Processing **10**, 266 (2001).

[48] S. Berg, D. Kutra, T. Kroeger, C. N. Straehle, B. X. Kausler, C. Haubold, M. Schiegg, J. Ales, T. Beier, M. Rudy, K. Eren, J. I. Cervantes, B. Xu, F. Beuttenmueller, A. Wolny, C. Zhang, U. Koethe, F. A. Hamprecht, and A. Kreshuk, Nature Methods **16**, 1226 (2019).

[49] W. E. Lorensen and H. E. Cline, in *Proceedings of the 14th annual conference on Computer graphics and interactive techniques - SIGGRAPH '87*, Vol. 21 (ACM Press, New York, New York, USA, 1987) pp. 163–169.

[50] D. Cohen-Steiner and F. Da, The Visual Computer **20**, 4 (2004).

[51] M. Kazhdan and H. Hoppe, ACM Transactions on Graphics **32**, 1 (2013).

[52] L. D. Landau and E. M. Lifshitz, *Fluid Mechanics, Second Edition: Volume 6 (Course of Theoretical Physics)*, 2nd ed., Course of theoretical physics / by L. D. Landau and E. M. Lifshitz, Vol. 6 (Butterworth-Heinemann, 1987).

[53] W. Zeng and X. D. Gu, *Ricci Flow for Shape Analysis and Surface Registration*, SpringerBriefs in Mathematics (Springer New York, New York, NY, 2013).

[54] U. Pinkall and K. Polthier, Experimental Mathematics **2** (1996), 10.1080/10586458.1993.10504266.

[55] N. Aigerman and Y. Lipman, ACM Transactions on Graphics **34**, 190:1 (2015).

[56] L. V. Ahlfors, *Lectures on Quasiconformal Mappings*, University lecture series (American Mathematical Society, 2006).

[57] M. Desbrun, A. N. Hirani, M. Leok, and J. E. Marsden, (2005), arXiv:0508341 [math].

[58] M. D. P. S. Keenan Crane, Fernando de Goes, in *ACM SIGGRAPH 2013 courses*, SIGGRAPH '13 (ACM, New York, NY, USA, 2013).

[59] M. Arroyo and A. Desimone, Physical Review E **79** (2009), 10.1103/physreve.79.031915.

[60] I. Nitschke, S. Reuther, and A. Voigt (Birkhäuser, Cham, 2017) pp. 177–197, arXiv:1611.04392.

[61] E. Efrati, E. Sharon, and R. Kupferman, Journal of the Mechanics and Physics of Solids **57**, 762 (2009).

[62] N. Romeo, A. Hastewell, A. Mietke, and J. Dunkel, eLife **10** (2021), 10.7554/eLife.68679, 2103.08130.

[63] G. Dalmasso, M. Musy, M. Niksic, A. Robert-Moreno, C. Badía-Careaga, J. J. Sanz-Ezquerro, and J. Sharpe, bioRxiv , 2021.12.16.472948 (2021).

[64] B. Lévy and H. R. Zhang, in *ACM SIGGRAPH 2010 Courses*, SIGGRAPH '10 (Association for Computing Machinery, New York, NY, USA, 2010).

[65] I. Jolliffe, *Principal component analysis* (Springer Verlag, New York, 2002).

[66] R. Reuter and M. P. Scott, Development **109**, 289 (1990).

[67] M. Bate and A. Martinez Arias, *The Development of Drosophila Melanogaster* (Cold Spring Harbor Laboratory Press, 2009) p. 1558.

[68] V. Hartenstein, en*Atlas of Drosophila Development* (Cold Spring Harbor Laboratory Press, 1993).

[69] R. Klapper, C. Stute, O. Schomaker, T. Strasser, W. Janning, R. Renkawitz-Pohl, and A. Holz, Mechanisms of Development **110**, 85 (2002).

[70] G. Wolfstetter, M. Shirinian, C. Stute, C. Grabbe, T. Hummel, S. Baumgartner, R. H. Palmer, and A. Holz, Mechanisms of Development **126**, 721 (2009).

[71] E. Rozbicki, M. Chuai, A. I. Karjalainen, F. Song, H. M. Sang, R. Martin, H.-J. Knölker, M. P. MacDonald, and C. J. Weijer, Nature Cell Biology **17**, 397 (2015).

[72] C.-J. Huang, C.-T. Tu, C.-D. Hsiao, F.-J. Hsieh, and H.-J. Tsai, Developmental Dynamics **228**, 30–40 (2003).